



# Variability of Jupiter’s Synchrotron Radiation: Goldstone Apple Valley Radio Telescope (GAVRT) Observations -II

K. Matuszewska<sup>1</sup>, T. Velusamy<sup>2</sup>, V. Adumitroaie<sup>2</sup>, J. Arballo<sup>2</sup>, R. Dorcsey<sup>1</sup>, S. Han<sup>3</sup> , E. Klopping<sup>1</sup>, N. Kreuser-Jenkins<sup>1</sup>, S. Levin<sup>2</sup>, and D. Santos-Costa<sup>4</sup> 

<sup>1</sup> Lewis Center for Educational Research, 17500 Mana Road, Apple Valley, CA 92307, USA; [thangasamy.velusamy@jpl.nasa.gov](mailto:thangasamy.velusamy@jpl.nasa.gov)

<sup>2</sup> Jet Propulsion Laboratory, California Institute of Technology, Pasadena, CA 91109, USA

<sup>3</sup> Marine Information Technology Corporation, Seoul, Republic Of Korea

<sup>4</sup> Space Science Department, Southwest Research Institute, San Antonio, TX, USA

Received 2022 March 4; accepted 2022 April 26; published 2022 August 3

## Abstract

Jupiter’s decimeter-wavelength flux density is dominated by synchrotron emission from magnetically trapped  $\sim 5\text{--}50$  MeV electrons in the radiation belts. Synchrotron radio emission remains the most useful diagnostic of the radiation belts, and a global picture is provided by ground-based observations. Monitoring of the long-term variations of Jupiter’s Synchrotron Radiation (JSR) flux density is crucial to understanding its relationship with the solar wind. The GAVRT (Goldstone-Apple Valley Radio Telescope) program operates two retired Deep Space Network (DSN) antennas, and as part of their K-12 program and Juno support, GAVRT has been collecting data to monitor JSR radio emission at 2280 MHz (13 cm wavelength). We present new results from 2019 August to 2021 December GAVRT monitoring observations. As viewed from Earth the JSR varies systematically (by about 10%) with Jupiter’s 9.9 hr rotation period, and our observations were typically much shorter than 9.9 hr. To estimate the daily flux density of JSR, we took advantage of recent progress in modeling the radiation belt, scaling individual observations by the predicted relative variation due to Jupiter’s rotation as viewed from Earth. We discuss the JSR variability from 2015 to 2021, combining our results with previous GAVRT data. Our new results show a marked decrease ( $\sim 1$  Jy) in JSR flux density between 2018 and 2021, while earlier observations showed an increase from 2015 to 2018. These results are remarkably consistent with long-term variability shown by the simulations of Han et al. based on models driven by the solar wind ram pressure.

*Unified Astronomy Thesaurus concepts:* [Radio astronomy \(1338\)](#); [Radio observatories \(1350\)](#); [Jupiter \(873\)](#)

## 1. Introduction

Jupiter’s radiation belts and synchrotron radiation (JSR) are major components of the planet’s magnetosphere. Constituting an excellent physical laboratory, they have drawn much attention for both in situ exploration (by Juno) and by remote sensing Earth observations. Characterizing the radiation belts still requires complex modeling, requiring validation by direct observations, including ground-based Earth observations. As part of their K-12 program, and Juno support, GAVRT (Goldstone-Apple Valley Radio Telescope) has been collecting data to monitor the JSR at 2280 MHz. The GAVRT program operates retired DSN antennas (DSS13 and DSS28) with NASA support, under a partnership between Jet Propulsion Laboratory (JPL), California Institute of Technology and the Lewis Center for Educational Research (LCER). The NASA-JPL Jupiter Patrol is a long-term radio astronomy monitoring program which began in 1971 (Klein 1975). Since the inception of the GAVRT program in 1996, it has continued the Jupiter patrol (Klein et al. 2001).

Recently, using the data from DSS13, Velusamy et al. (2020 hereafter referred to as Paper I) derived JSR flux densities at

multiple epochs, and showed an increasing trend in JSR flux from 2015 to 2018, consistent with models for the magnetospheric solar wind interactions. Here, we present new results from 2019 to 2021 GAVRT monitoring observations, continuing a long-term variability analysis of JSR flux density. The results presented here allow comparison, in this Juno era, to remote sensing data from the Microwave Radiometer (MWR, Janssen et al. 2017) and to in situ data from the Juno fields and particles instruments (e.g., Bagenal et al. 2017; Nichols et al. 2020). See Paper I for further discussion.

Jupiter’s synchrotron radiation at GAVRT wavelengths (13 cm), measures the non-thermal flux emitted by  $\sim 10$  MeV relativistic electrons trapped in Jupiter’s radiation belts. As noted in Paper I and elsewhere (e.g., de Pater 1980; de Pater & Klein 1989), changing viewing geometry caused by the rotation of Jupiter results in systematic variation of the JSR, known as the “beaming curve”. GAVRT Jupiter observations on a given day are typically short, only a few hours long, during school hours when students take data. Typical observations consist of flux density measurements corresponding to only a few longitudes, insufficient to observationally determine the

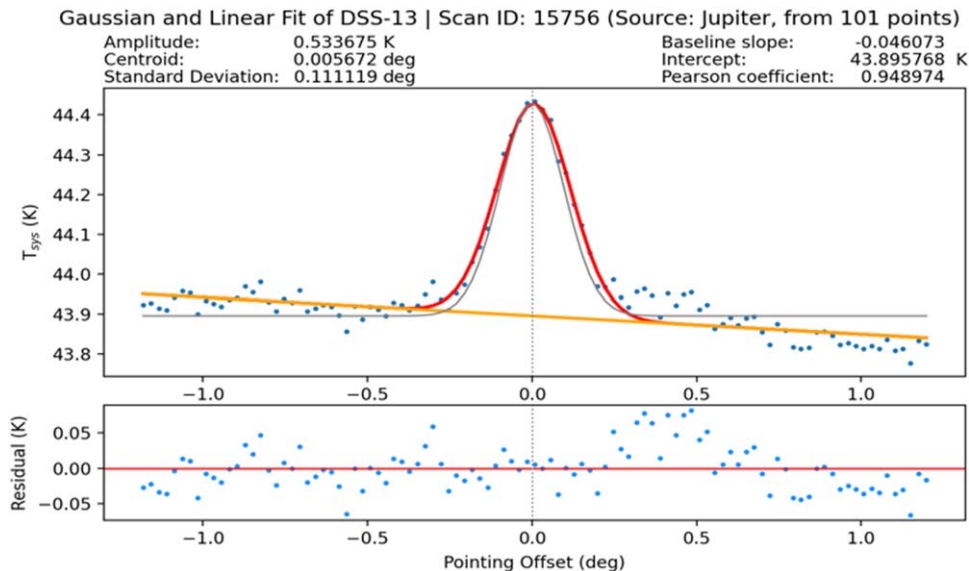


**Figure 1.** GAVRT scan data. Observation consisted of scans across either Jupiter or a calibration source, sampling the radiometer output at 1 s intervals (about 10 samples per beamwidth). The source antenna temperature ( $T_A$  K) is measured by fitting a Gaussian beam shape. (upper panel): scan data are shown as dots. Orange line: fit to the baseline. Red line: Gauss fit to source with baseline. Gray line: Gauss fit to source with averaged, flat baseline. The scan- fit parameters are listed on top. The standard deviation corresponds to the fitted beam size,  $0.424 \times \text{FWHM}$ . (lower panel): Gauss fit residuals.

beaming curve. However, it is still possible to estimate the intrinsic JSR flux density by applying a scaling factor to correct for viewing geometry, as characterized by a pre-determined “normalized beaming curve” which models the 9.9 hr variation independently of the total emission. For the analysis presented in this paper, we use normalized model beaming curves for each day’s Earth viewing geometry derived using the Adumitroaie (2020) framework to simulate JSR using electron distributions and Jovian magnetic field models. As discussed in Paper I, these model beaming curves were found to be consistent with those observed in the GAVRT data. This approach allows us to estimate a single-day intrinsic JSR flux density without taking data over a full rotation.

The observations (2019 August–2021 December) and flux density calibrations are described in Section 2. The analysis and estimate of daily JSR flux densities are described in Section 3. The long-term JSR variability (2015 March–2021 December) in the GAVRT data is discussed in Section 4. Another focus in this paper is to provide an update on the GAVRT data and opportunities for citizen science monitoring of JSR. We note that the first author of this paper started this work as a senior at Ribet Academy high school and has continued after graduation.

## 2. Observations

The observations were made between 2019 August and 2021 December, using the DSS13 34 m radio telescope and the  $S$ -band receiver operating at 2.280 GHz (13 cm wavelength) over

a bandwidth of 40 MHz. Teachers and students from several schools participated on many of the days. GAVRT team members (Nancy Kreuser-Jenkins and Ethan Klopping) at LCER continued taking data monitoring Jupiter even when students could not be present. See acknowledgements for a list of participating schools and students.

As described in Paper I, a typical session of Jupiter observations lasted 2–4 hr, although they varied from day to day. Any individual observation comprised a pair of scans, typically 2 minutes in duration, either across Jupiter or across a calibration source, along decl. (dec) and along cross-decl. (x-dec). The slewing rate was  $1^\circ 2 \text{ minute}^{-1}$ , sampled once per second, with sufficient data collected off-source to allow fitting for drifts. Figure 1 shows an example of scans across Jupiter.

The peak antenna temperature and beamwidth were measured by simultaneously fitting a baseline and a Gaussian profile as demonstrated in Figure 1. The fit gives a robust estimate of the source antenna temperature,  $T_A$  (K), with a good fit to the baseline and typical  $1\sigma$  rms noise of  $\sim 0.02$  K. The DSS-13  $S$ -band receiver is a total power radiometer, potentially susceptible to atmosphere and temperature changes. As a result, the scan data occasionally show drift in the baseline (Figure 1). Some bad scans are therefore expected, especially on weak sources such as Jupiter. However, in most cases a quadratic baseline fit works well to remove drifts. Scans for which baselines were too steep, data too noisy, or with too few points to reliably fit a Gaussian, were rejected. Other criteria for excluding scans were Gaussian fits with off-center centroids (poor pointing), or with inconsistent beam shape. The semi-

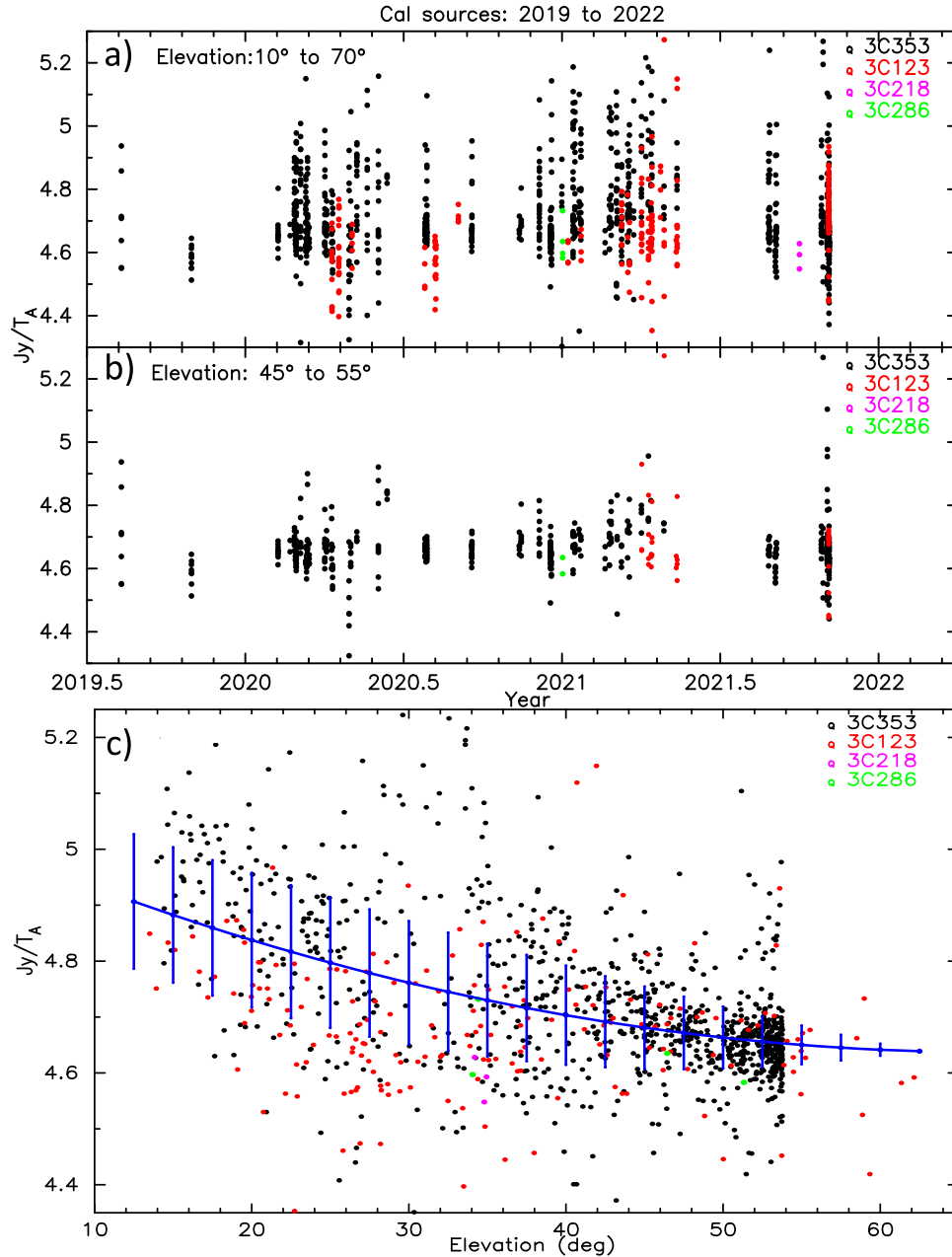


**Figure 2.** The antenna system calibration. Plots of  $S(Jy)/T_A(K)$  antenna temperature to flux density conversion factor ( $F_{Jy}$ ) and delineating elevation dependence. (a) all elevation data plotted against time. (b) selected elevation range 45–55 deg data plotted with time to show the conversion factor did not vary over time. (c) all  $F_{Jy}$  values plotted against elevation; the blue line shows a fit for the elevation dependence and the error bars show the uncertainties, which are  $<2\%$ .

automated algorithm used for fitting the raw scan data flagged extremely bad scans using the above criteria. Any bad scans still present in the data set were examined during further analysis (as discussed in Section 3).

On most days, 3C353 and/or 3C123 were observed as calibration sources. On a few days, 3C218 and 3C286 were also observed (see Figure 2(a)). From each calibration source (CAL) scan observation we derive the antenna temperature,

which is used for the flux density conversion factor, defined as  $F_{Jy} = S(Jy)/T_A(K)$ . For calibration sources, we use the flux densities as given in Paper I Table 1, which is based on the Perley & Butler (2017) flux density scale. In Figure 2, the measured flux conversion factor for each scan is plotted (i) as a function of time in (a) and (b) and (ii) as function of source elevation in (c). As seen in Figure 2(b),  $F_{Jy}$  derived from all calibration source elevations between 45° and 55° is

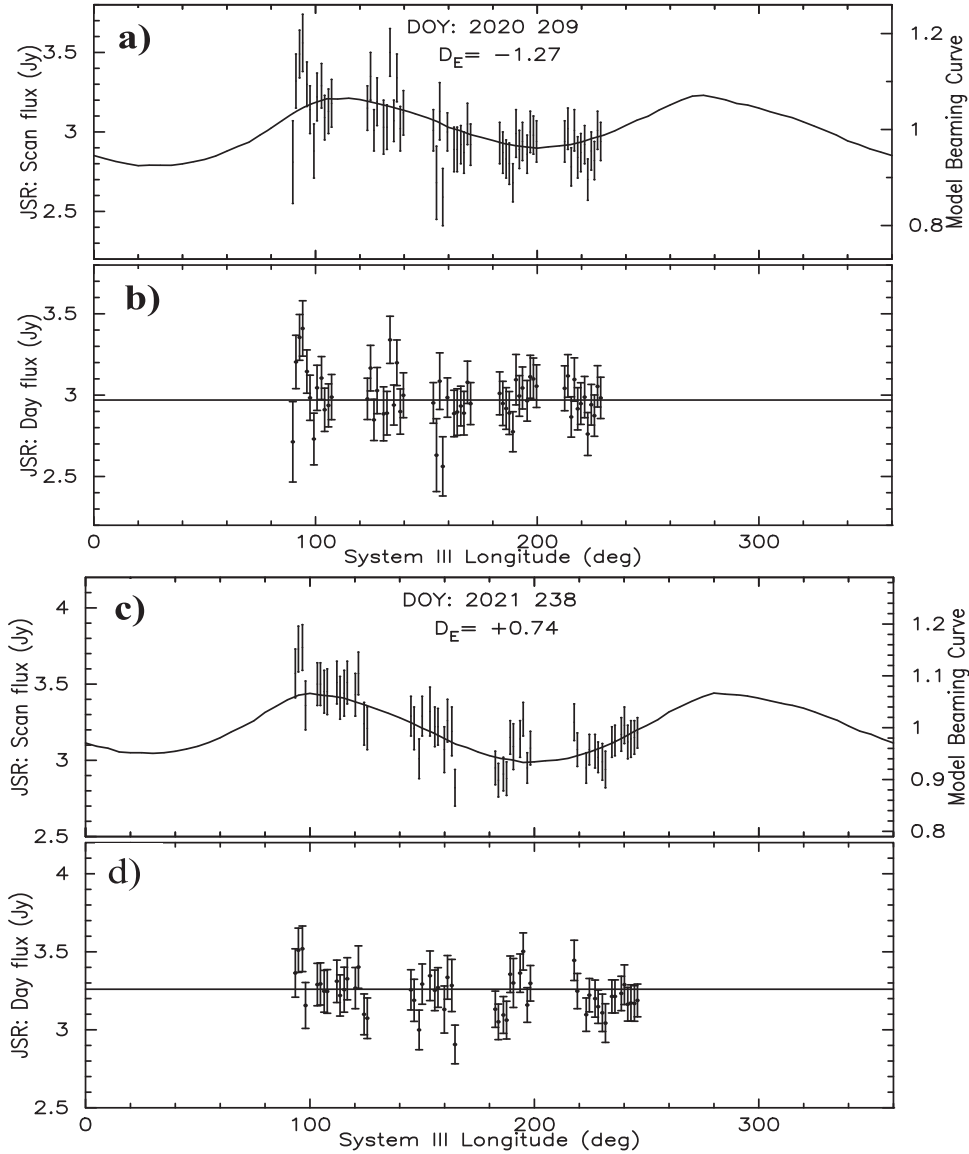


**Figure 3.** (a) and (c) Example of one day’s JSR scan flux density data (GAVRT scan flux densities observed on 2020 DOY 209 (July 27) and 2021 DOY 238 (August 26)). Observed JSR scan flux densities (data points with error bars) and model beaming curve (solid line) are shown as a function of longitude. Note the modulation of flux density with Jupiter’s rotation. (b) and (d) JSR day fluxes estimated from each scan after correcting for the modulation (Equation (2)). Intrinsic day flux for each day is estimated by averaging all observed scans after excluding any outliers, if present.

consistently within a range of 4.6–4.7, while Figure 2(a) shows a large scatter when all elevations are considered. We conclude that the scatter in Figure 2(a) is a result of elevation dependent variation of  $F_{Jy}$ . Indeed, as seen Figure 2(c), a weak elevation dependent variation from 4.65 at high elevation to 4.9 at low elevation seems to fit the data. We use a 2nd degree polynomial fit of the form:

$$F_{Jy}(\varphi) = a_0 + a_1 * (\varphi - 50) + a_2 * (\varphi - 50)^2 \quad (1)$$

where  $\varphi$  is elevation in degrees,  $a_0 = 4.643 \pm 0.008$ ;  $a_1 = -0.0026 \pm 0.0010$ ;  $a_2 = 0.0001 \pm 0.00003$ .

As noted in Paper I, the near constant scan-to-scan value of  $F_{Jy}$  suggests that the recorded system antenna temperatures (Figure 1) are well calibrated in degrees Kelvin (K). For each Jupiter scan, the fitted antenna temperature ( $T_A$ ) as seen in Figure 1 is converted to flux density (Jy) by applying the  $F_{Jy}$  conversion factor for the scan elevation using Equation 1. The uncertainty in the scan flux densities is estimated from the measurement uncertainty in  $T_A$  and the uncertainty in the conversion factor as indicated in Figure 2(b). All our calibration sources are commonly used and known to have

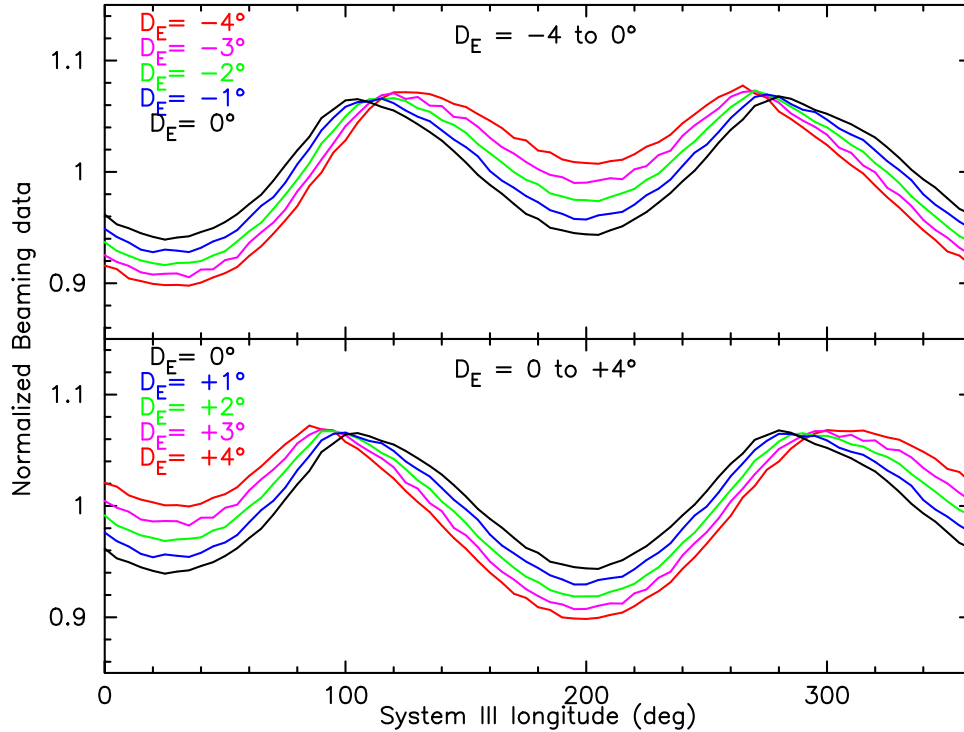


**Figure 4.** Examples of model Beaming curves  $S_{\text{mod}}(\lambda_{\text{III}}, D_E)$  derived by Adumitroaie (2020). The Earth declinations are differentiated by the colors as marked. We use them for estimating the daily JSR flux density from the measured scan fluxes corrected for beaming modulation.

stable flux densities,  $\sim 1\%$  level (Perley & Butler 2017). Also, the overall consistency of the flux to antenna temperature conversion factor,  $F_{Jy}$ , among different calibration sources in GAVRT observations since 2015 seem to further confirm their stability.

### 3. Estimating Daily JSR Flux Densities

As the first step for analyzing the intrinsic daily JSR flux density, we compile the Jupiter ephemeris for each scan time on all observation days. We used the NASA/JPL Horizons On-Line Ephemeris System, (<https://ssd.jpl.nasa.gov/horizons/>) (Giorgini et al. 1996) for Jupiter’s, sky position, distance, sub-lon and sub-lat at each scan time. The Horizon’s sub-lon and sub-lat correspond to System III longitude ( $\lambda_{\text{III}}$ ) and jovigraphic Earth decl. ( $D_E$ ), respectively. However, for most of our analysis presented here we need to use jovicentric latitude ( $D_E$ ). Therefore, we converted the Horizons  $D_E$  values to jovicentric by using the relationship in Dulk et al. (1997):  $D_E$  (jovicentric) = 0.87  $D_E$  (jovigraphic, from Horizons). In all our analysis we use jovicentric values for  $D_E$ .

Because the distance to Jupiter changes with time, we normalize the observed flux densities to a standard distance of 4.04 au by applying an inverse square distance correction, using the distance to Jupiter on each day of observation. The normalized scan flux densities include both the thermal and

non-thermal components of Jupiter’s radiation. Synchrotron emission in its entirety is non-thermal radiation which varies with Jupiter’s rotation, while the thermal radiation remains fixed (with flux density of 2.02 Jy at the GAVRT wavelength (de Pater & Massie 1985), at the standard distance of 4.04 au). The JSR flux density for each scan is then obtained by subtracting 2.02 Jy from the normalized scan flux densities. Using ephemeris data for each scan time, the corresponding System III longitude ( $\lambda_{\text{III}}$ ) and Earth decl. ( $D_E$ ) are then assigned to the measured JSR scan flux density,  $S_{\text{scan}}$  in Jy, as  $S_{\text{scan}}(\lambda_{\text{III}}, D_E)$ . Example plots of scan JSR flux densities observed on two different days are shown in Figure 3. GAVRT scan flux densities for all days observed after 2015 are presented in the supplementary data (available online at [stacks.iop.org/PASP/134/084401/mmedia](https://stacks.iop.org/PASP/134/084401/mmedia)) file and are also available at <https://gavrt.lewiscenter.org/>. In this file, the observed scan flux densities for the period 2019 to 2021 (reported in this paper), and for 2015 to 2018 (presented in Paper I) are listed in two data sheets. Because of the beaming effect (see below) the JSR flux density measurement in a single Jupiter scan cannot be regarded as the intrinsic JSR flux density on the given day. Here, we describe how we can estimate the intrinsic day flux density accounting for the beaming effect.

As noted in Paper I, the varying viewing geometry caused by Jupiter’s 9.9 hr rotation combines with the geometry of

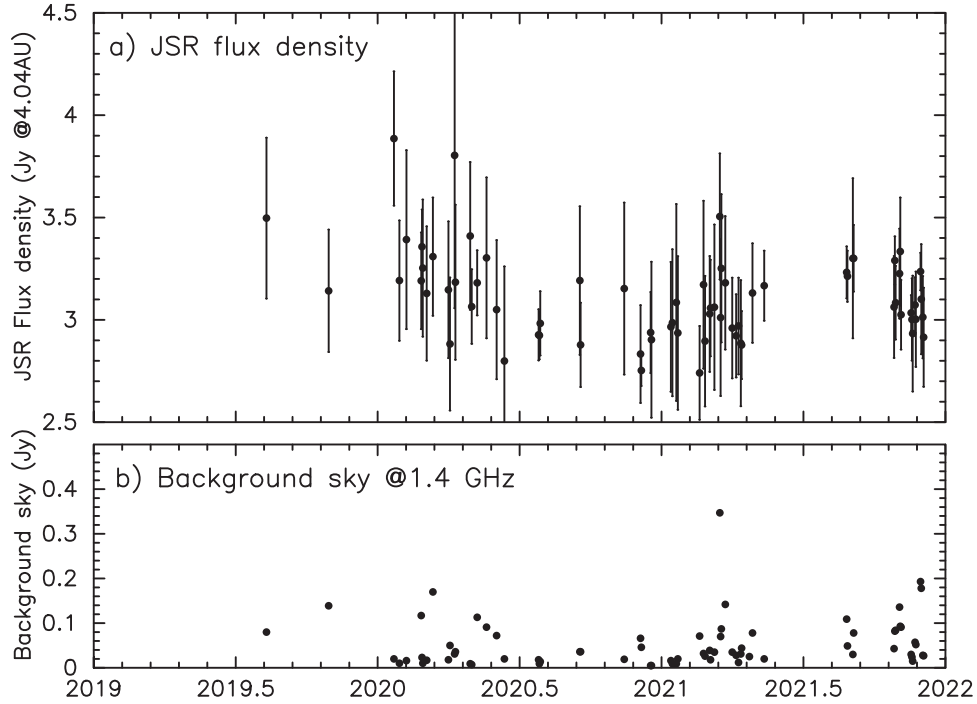


**Figure 5.** (a) GAVRT measurements of JSR flux densities derived from single day observations during 2019 August–2021 December. (b) Background flux density at the sky location of Jupiter on the days of observation, estimated from the NVSS point source catalog. Note the expanded flux density scale. The sky background contribution is significantly small and therefore, observed JSR variability is real.

Jupiter’s magnetic field and the highly beamed nature of synchrotron emission to produce a systematic variation in the JSR flux density, known as the “beaming curve” (e.g., Roberts & Komesaroff 1964; Carr et al. 1983). Because the 13 cm wavelength GAVRT antenna beam ( $13'6$ ) is much larger than JSR source (size less than  $2'$ ) the measured flux densities correspond to synchrotron emission from the entire radiation belt (up to radius  $\sim 3R_J$ ) and therefore any short-term variation observed is determined by viewing geometry corresponding to Jupiter’s central meridian longitude as seen by the observer or the System III longitude ( $\lambda_{\text{III}}$ ). With long duration ( $>9.9$  hr) observations which cover Jupiter’s full rotation, we could derive the beaming curve using the observed JSR scan flux densities and estimating the intrinsic JSR day flux density is straightforward. On the other hand, the GAVRT observations presented in this paper do not include such long-duration observing sessions. In principle, we could combine several days data to derive a mean beaming curve, as done in Paper I. Instead, we use a different approach, taking advantage of recent developments in modeling the radiation belts. A new set of beaming curves is generated via a synchrotron radiation model currently used to predict (for the Juno mission) the in-situ signature of the Jovian radiation belts, as described in Santos-Costa et al. (2017). This simulation framework delivering the Stokes parameters of the synchrotron emission relies on pre-computed or assumed electron distributions and a Jovian

magnetic field model. Here, the electron distribution is obtained from a high-fidelity physics-based code for modeling the inner Jovian electron radiation belts (Santos-Costa & Bolton 2008). Furthermore, these JSR results are based on the JRM09 magnetic field model (Connerney et al. 2018) along with a set of ancillary parameters ( $M$ -shell and  $B_{\text{crit}}$ ) (Adumitroaie et al. 2019).  $M$ -shell is defined similarly to  $L$ -shell, but for a non-dipolar field. Here,  $M$ -shell refers to the distance from the center of Jupiter in Jovian radii at the minimal field strength on the field line, using the JRM09 magnetic field model (Connerney et al. 2018) with the Jovian current sheet included (Connerney et al. 1981).  $B_{\text{crit}}$  is defined as the minimum magnetic field amplitude for a given  $M$ -shell at which electrons that mirror at or below the upper boundary of the atmosphere are lost (Divine & Garrett 1983). Continuing this approach of Adumitroaie (2020) and Adumitroaie et al. (2016) we calculated the JSR beaming curves for an Earth-based observer decl.,  $D_E = -4^\circ$  to  $+4^\circ$  at intervals of  $0.5^\circ$ . Examples of the model beaming curves are shown in Figure 4. These model beaming curves at selected  $D_E$  have been found consistent with GAVRT data reported in Paper I, validating their use in our present analysis.

Figure 3 shows examples of measured JSR scan flux densities as a function of System III longitude (representing Earth view geometry) for two selected days with the longest observing session (typically, on other days the number of

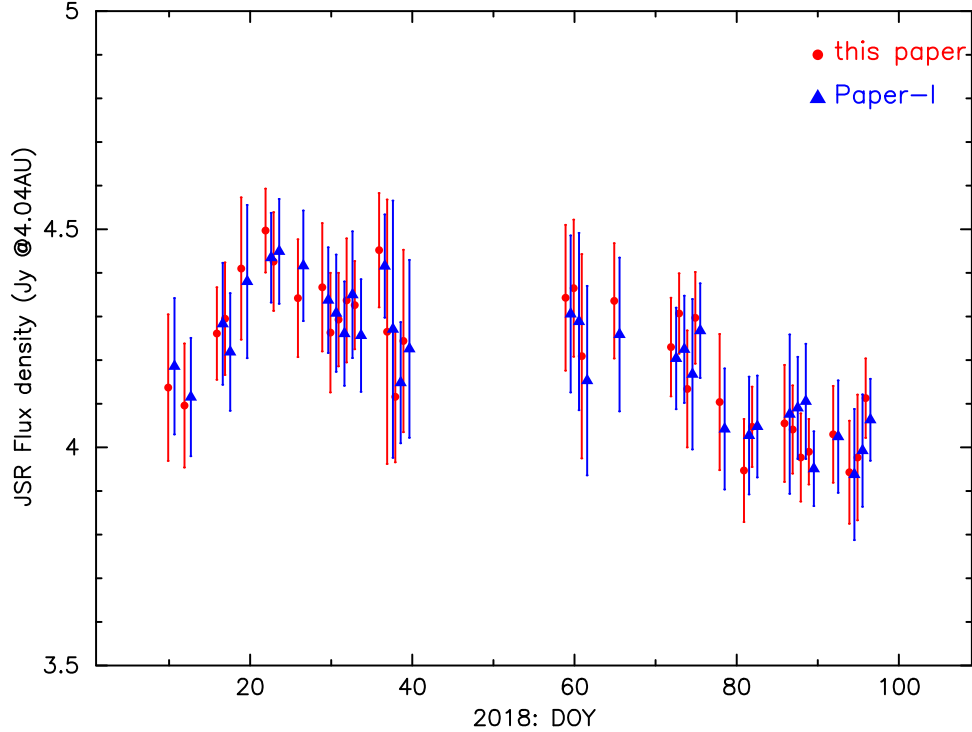


**Figure 6.** GAVRT JSR day flux densities for the 2018 data (January 8–April 6). The published data from Paper I are shown in blue (triangle). The points in red (dot) are new estimates of flux densities using the model beaming curves (this paper). For clarity the points for each day are plotted with slight DOY offset between them.

scans, therefore the longitude coverage, is even more sparse). Even this longitude coverage is not adequate to derive a beaming curve observationally. Therefore, we use the model beaming curves described above. First, we generate the beaming curve corresponding to the Earth decl. ( $D_E$ ) for the day of the observation by interpolating from the family (library) of beaming curves available for  $D_E = -4^\circ$  to  $+4^\circ$  at intervals of  $0.5^\circ$ . To illustrate this in Figure 3, we overplot the normalized model beaming curve ( $S_{\text{mod}}(\lambda_{\text{III}}, D_E)$ ) on the observed JSR scan flux densities ( $S_{\text{scan}}(\lambda_{\text{III}}, D_E)$ ). Though sparsely sampled in longitude the observed data points seem to be consistent with the scaled up normalized model beaming curve. Practically, this scaling factor is the measure of the intrinsic value of the JSR day flux density. In other words, we can estimate the JSR day flux density from each scan flux density measurement as:

$$S_{\text{day}} = S_{\text{scan}}(\lambda_{\text{III}}, D_E) / S_{\text{mod}}(\lambda_{\text{III}}, D_E) \quad (2)$$

A plot of the scan-by-scan estimate of the day flux is plotted in panels (b) and (d) of Figure 3. Averaging scan by scan estimates provides a robust estimate (as indicated by horizontal lines in Figures 3(b) and (d)). Note this approach allows estimating the daily flux with fewer scans observed each day, and even with just a few hours data, without the necessity of taking data over one full rotation. Any large deviation of any particular scan data from the average in Figures 3(b) and (d), if

present is likely to be result of a bad scan, either due to pointing or system performance. Though the semi-automated algorithm used for fitting the raw scan data flags out extremely bad scans, some bad scans are still present in the processed data and are identified in plots similar to those in Figure 3, before averaging individual scan estimates.

Following our new approach as described above, we estimated the intrinsic JSR day flux density for all available days of Jupiter observation between 2019 August and 2021 December. In Figure 5(a) the JSR day flux density is plotted over time. For each day the estimated flux density and associated uncertainty are shown. The JSR variability observed during this period is very significant, especially the decrease in the flux density in 2020 compared to the 2018 data presented in Paper I (see Section 4).

While interpreting the variability one must consider possibilities of contamination from background sky contribution at Jupiter’s position. As described in Paper I, this contribution is small in our data set due to the use of scanning observations and we quantify background source contributions using the 1.4 GHz NRAO VLA Sky Survey (NVSS), found in (Condon et al. 1998). We computed sky contribution by adding all point sources (beam weighted) within the beam. Estimated contributions are plotted in Figure 5(b). It may be noted that we do not correct the JSR flux densities for the sky background contribution. Nevertheless, the estimated sky contribution,

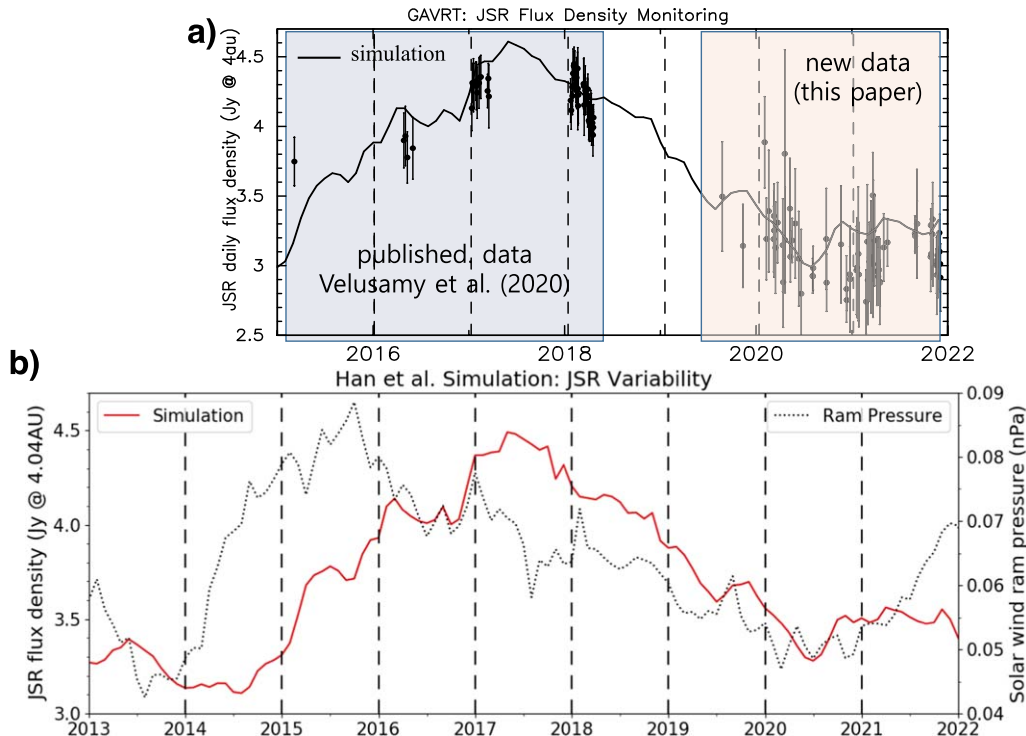


**Figure 7.** (a) GAVRT monitoring of Jupiter’s synchrotron radiation (JSR) during 2015–2022. Measured daily JSR flux densities are plotted as a function of DOY for each year. The data for 2019–22 are from the observations reported here. The data for 2015–18 are reproduced from Paper I (see supplementary data file). Long-term JSR variability simulation (see below) overplotted on GAVRT data to show their similarities. (b) Long-term JSR variability simulation by Han et al. (2018) overplotted on long-term variability of solar wind ram pressure at Jupiter’s orbit estimated using Tao et al. (2005) magnetohydrodynamic simulation. Note the results for 2018–2022 are from a recent simulation using the same approach discussed by Han et al.

Figure 5(b), illustrates that the variability in Figure 5(a) is real and is not significantly affected by background contribution. The estimated background contribution is typically low,  $\ll 0.2$  Jy with the only exception for 2021 DOY 75 at 0.35 Jy. Furthermore, this estimate of sky background is at 1.4 GHz and the extrapolated sky contribution at the GAVRT receiver frequency (2.28 GHz) is expected to be at a much lower level, despite an increase with distance normalization to 4.04 au.

Finally, to further validate our new approach for deriving the JSR day flux densities, we reprocessed the GAVRT 2018 data, using the same approach with model beaming curves. It may be noted that day fluxes for 2018 presented in Paper I used mean beaming curves derived using observations over a period of several weeks and then estimating the day flux densities from the residual scan flux densities for each day. In Figure 6 we compare the day fluxes as reported in Paper I with those derived using the model beam curves as used in the present work. The remarkable degree of agreement between the two data sets is further proof of our method as well as a validation of our model beaming curves.

This technique relies on the assumption that the beaming curve is predominantly caused by viewing geometry of the

magnetic field (Dulk et al. 1999), neglecting any effect caused by variation of the electron distribution with longitude on timescales of the rotation period. In other words, our technique assumes there are no time-dependent longitudinal asymmetries in the electron distributions during and between observation days. This is a safe assumption and works well under normal circumstances, except in extremely rare situations of surface impacts (e.g., July 1994: de Pater et al. 1995; July 2009: Santos-Costa et al. 2011) that are known to cause highly longitudinal asymmetries. However, such extreme situations are easily identifiable and excluded from our analysis.

#### 4. JSR Time Variability and Solar Wind Interaction

Synchrotron emission processes (including radial transport) vary over a wide range of timescales. It is important to monitor long-term changes in the JSR in order to study how it relates to the solar wind and solar activity in general (see Bolton et al. 1989). GAVRT JSR day flux densities for all days observed after 2015 are presented in the supplementary data file and are also available at <https://gavrt.lewiscenter.org/>. In this file, the observed day flux densities for the period 2019 to 2021 (reported in this paper), and for 2015 to 2018 (presented in Paper I) are listed in two data sheets. Paper I presented GAVRT

observations of JSR variability from 2015 to 2018, showing a JSR flux density increase from 2015 March to 2018 April. To further investigate the times scales in JSR variability on a longer time baseline, in Figure 7(a) we show our present results along with those previously published to cover a period from 2015 March to 2021 December. Most interestingly, the JSR flux density in 2020 shows a marked decrease of  $\sim 1$  Jy from its 2018 level. Unfortunately, GAVRT did not have much coverage between 2018 and 2019 to characterize the decrease as sudden or gradual. The two isolated measurements in 2019 seem to suggest it could have been a gradual decrease. Nevertheless, the new GAVRT results are very significant to our understanding of the long-term variability, showing a clear pattern of slow increase from 2015 to 2018 and then a decrease from 2018 to 2022. It is intriguing that this variability pattern is most likely related to the solar activity cycle. Though GAVRT data were observed at different  $D_E$  ( $-3^\circ$  to  $+1^\circ$ ), as discussed by Dunn et al. (2003), Sicard et al. (2004) and Santos-Costa et al. (2008),  $D_E$  is likely to have negligible effect on the long-term variability. Indeed, as seen from Figure 7(b) the GAVRT variability is consistent with the simulations as induced by Solar wind interactions (Han et al. 2018).

Analysis of EUV data monitoring the Io plasma torus by the EXCEED (Extreme ultraviolet spectroCope for Exospheric Dynamics) spectrometer on board the HISAKI satellite (Yamazaki et al. 2014; Yoshikawa et al. 2014) has shown that the changes in solar wind ram pressure drive fluctuations of the dawn-to-dusk electric field in the Jovian magnetosphere (Murakami et al. 2016). Recently, Han et al. (2018) have investigated the temporal variations of JSR, modeling the influence of a fluctuating dawn-to-dusk electric field on the radiation belt invoking radial diffusion model constraints. Their model introduced a time-varying diffusion coefficient dependent on solar wind ram pressure while retaining the coefficient which accounts for solar UV heating of Jupiter’s upper atmosphere. The ram pressure is determined by extrapolating the value at Earth’s orbit to that of Jupiter using magneto-hydrodynamic simulations (Tao et al. 2005).

In Figure 7(b) we reproduce the results on JSR variability for the period 2013–2018 from Han et al. (2018) along with a new calculation extending their simulation to 2022. The simulated JSR variability is overplotted with the solar wind ram pressure at Jupiter’s orbit. It may be noted that because of the large timescales (1–2 yr) for JSR response to solar wind, and our interest only in the long-term JSR variability, the solar wind ram pressure data have been averaged over a six month period. To track the time history of solar wind at Jupiter’s orbit, in Figure 7(b) we include the solar wind ram pressure data and simulation from 2013, two years prior to GAVRT monitoring observations reported here. One can notice that the GAVRT variability data (Figure 7(a)) agrees remarkably well with the simulations of Han et al. (Figure 7(b)). On one hand, the solar wind ram pressure increases sharply to its maximum value in

2016 and decreases gradually afterwards. On the other hand, the maximum of JSR can be found in the middle of 2017. This highlights the time lag of  $1 \sim 2$  yr between the pressure and JSR suggested by Bolton et al. (1989), which is one of the key features of long-term variations of JSR. Thus, our results seem to confirm that the dawn-to-dusk electric field associated with solar wind conditions drives long-term variations of JSR. Furthermore, the good agreement between observed and simulated variability for years 2015–2022 provides new constraints on the model parameters used by Han et al. especially for the radial diffusion determining the timescales for the long-term variability.

In their approach, Han et al. (2018) assumed the lower limit of the diffusion coefficient for solar UV heating of Jupiter’s upper atmosphere (i.e.,  $D_{LL}(UV) = 3.0 \times 10^{-10} L^3$ ) because the model favors the slower diffusion process to better reproduce the aforementioned time lag. Analyzing Jovian Auroral Distributions Experiment (JADE) (McComas et al. 2017) and Jupiter Energetic-particle Detector Instrument (JEDI) (Mauk et al. 2017) data will help put constraints on the range of the diffusion coefficient, thereby testing the assumption of the model.

Finally, GAVRT results demonstrate that the Han et al. model is indeed a powerful tool for long-term JSR variability as it reproduces well the observations. The ram pressure for the years 2020–2022 (Figure 7(b)) shows marked increase beyond 2021. Based on the 1–2 yr lag as suggested by the simulations, we can expect the JSR flux density to show an increasing trend in the 2022–24 time frame. Future GAVRT monitoring of JSR will provide further constraints on modeling Jupiter’s radiation belts and variability of its synchrotron radiation.

## 5. Conclusions

In this paper we presented new results from analyzing the data observed during 2019 August–2021 December under the GAVRT program designed to monitor Jupiter with teacher-student participation. This work is a continuation of the GAVRT work reported in Paper I, by Velusamy et al. (2020). Here, we presented results using observations made at irregular intervals of time and with few scans on a given day. To estimate JSR flux density on a day-to-day basis we used a novel approach that uses the model beaming curves to correct JSR flux density measured by each scan for the brightness modulation with Jupiter rotation. This approach allows estimating the daily flux with fewer scans observed each day, without the necessity of taking data over one full rotation. This could open a new opportunity to study JSR variability using data collected by other antennas with far too few scans observed on each day, for example with the DSS 28 antenna at 3.1 GHz. Finally, GAVRT results for 2019–2022 show a marked decrease in JSR flux from its 2018 value. Furthermore, GAVRT data show JSR flux density increasing (2015–2018)

and decreasing (2018–22) trends. GAVRT variability data seem consistent with long-term variability simulated by models for the response of the radiation belts to solar radiation and solar wind. In particular, the data are consistent with the simulated temporal variations of JSR obtained by modeling the influence of a fluctuating dawn-to-dusk electric field on the radiation belt driven by solar wind ram pressure (Han et al. 2018). The solar wind data for 2020–22 suggest an increasing trend for JSR flux density in the 2022–24 time frame and future GAVRT monitoring of JSR will be very useful. The observations presented in this paper demonstrate the GAVRT Jupiter monitoring program serving as a citizen science opportunity to do science research.

We thank an anonymous referee for critical comments and suggestions that improved the discussion significantly. We thank Dr. C. Tao for providing magnetohydrodynamic solar wind data for JSR simulations. We acknowledge the support of Lisa Lamb, President/CEO and LCER staff for all their infrastructure and observational support to data presented in this paper. This work was performed in part at the Jet Propulsion Laboratory, California Institute of Technology, under contract with the National Aeronautics and Space Administration. Data were collected with the assistance of the following teachers and students:

St. Mary’s School Medford, OR Teacher—Holly Bensel  
 Canberra Japanese HS Canberra, Australia Teacher—Shinji Horiuchi  
 Komagane Tech HS Japan Teacher—Atsushi Hayashi  
 Newport MS Newport, PA Teacher—Peggy Olson  
 Cardinal Gibbons HS Raleigh, NC Teacher—Diane Ripollone  
 Newsome Sr. HS Lithia, FL Teacher—Scott Coonfare (students—Samantha Dolski/Sarah Dudjak)  
 Culver City HS Culver City, CA (student—Alex Cordova)  
 Irvine HS Irvine, CA (students—Swetha Palakur/Ria Singh)  
 Ribet Academy Los Angeles, CA (student—Klara Matuszewska)  
 Paloma Valley HS Menifee, CA Teacher—Joe Jennings  
 Broadwater Academy Exmore, VA Teacher—Elizabeth Hall (student—Ture Gustafson)  
 Ken Caryl MS Littleton, CO Teacher—Shelly Grandell

## ORCID iDs

S. Han  <https://orcid.org/0000-0003-1652-5365>  
 D. Santos-Costa  <https://orcid.org/0000-0003-0384-5255>

## References

- Adumitroaie, V. 2020, in American Geophysical Union, Fall Meeting 2020 (Washington, DC: AGU)
- Adumitroaie, V., Juno’s MWR Science Team, et al. 2019, in IEEE Aerospace Conf. (Piscataway, NJ: IEEE)
- Adumitroaie, V., Levin, S. M., Santos-Costa, G. S., & Jansen, M. A. 2016, in 2016 IEEE Aerospace Conf. (Piscataway, NJ: IEEE)
- Bagenal, F., Adriani, A., Allegrini, F., et al. 2017, *SSRv*, **213**, 219
- Bolton, S. J., Gulkis, S., Klein, M. J., de Pater, I., & Thompson, T. J. 1989, *JGR*, **94**, 121
- Carr, T. D., Desch, M. D., & Alexander, J. K. 1983, *Physics of the Jovian Magnetosphere*, (A83-26611 10-91) (Cambridge: Cambridge Univ. Press), 226
- Condon, J. J., Cotton, W. D., Greisen, E. W., et al. 1998, *AJ*, **115**, 1693C
- de Pater, I. 1980, *A&A*, **88**, 175
- Connerney, J. E. P., Acuna, M. H., & Ness, N. F. 1981, *JGR*, **86**, 8370
- Connerney, J. E. P., Kotsiaros, S., Oliverson, R. J., et al. 2018, *GeoRL*, **45**, 2590
- de Pater, I., Heiles, C., Wong, M., et al. 1995, *Sci*, **268**, 1879
- de Pater, I., & Klein, M. J. 1989, NASA Special Publication, Sp-494, 139D
- de Pater, I., & Massie, S. T. 1985, *Icarus*, **62**, 143
- Divine, N., & Garrett, H. B. 1983, *JGRA*, **88**A9, 6889
- Dulk, G. A., Leblanc, Y., Sault, R. J., Ladreiter, H. P., & Connerney, J. E. P. 1997, *A&A*, **319**, 282
- Dulk, G. A., Leblanc, Y., Sault, R. J., et al. 1999, *A&A*, **347**, 1029
- Dunn, D. E., de Pater, I., & Sault, R. J. 2003, *Icarus*, **165**, 121
- Giorgini, J. D., Yeomans, D. K., Chamberlin, A. B., et al. 1996, *BAAS*, **28**, 1158
- Han, S., Murakami, G., Kita, H., et al. 2018, *JGRA*, **123**, 9508
- Janssen, M. A., Oswald, J. E., Brown, S. T., et al. 2017, *SSRv*, **347**, 47
- Klein, M. J., Bolton, S. J., Gulkis, S., et al. 2001, in “Planetary Radio EmissionsV”, Proc. 5th International Workshop (Austria: OAW)
- Klein, M. J. 1975, *Nature*, **253**, 102
- Mauk, B. H., Haggerty, D. K., Jaskulek, S. E., et al. 2017, *SSRv*, **213**, 289
- McComas, D. J., Alexander, N., Allegrini, F., et al. 2017, *SSRv*, **213**, 547
- Murakami, G., Yoshioka, K., Yamazaki, A., et al. 2016, *GRL*, **43**, 12,308
- Nichols, J. D., Allegrini, F., Bagenal, F., et al. 2020, *JGRA*, **125**, e2020JA027904
- Perley, R. A., & Butler, B. J. 2017, *ApJS*, **230**, 7P
- Roberts, J. A., & Komesaroff, M. M. 1964, *Nature*, **203**, 827
- Sicard, A., Bourdarie, S. A., Krupp, N., et al. 2004, *AdSpR*, **33**, 2030
- Santos-Costa, D., Adumitroaie, V., Ingersoll, A., et al. 2017, *GeoRL*, **44**, 8676
- Santos-Costa, D., & Bolton, S. J. 2008, *P&SS*, **56**, 326
- Santos-Costa, D., Bolton, S. J., Sault, R. J., Thorne, R. M., & Levin, S. M. 2011, *JGR*, **116**, A12236
- Santos-Costa, D., Bolton, S. J., Thorne, R. M., Miyoshi, Y., & Levin, S. M. 2008, *JGR*, **113**, A01204
- Tao, C., Kataoka, R., Fukunishi, H., Takahashi, Y., & Yokoyama, T. 2005, *JGR*, **110**, A11208
- Velusamy, T., Adumitroaie, V., Arballo, J., et al. 2020, *PASP*, **132**, 4402V, (Paper I)
- Yamazaki, A., Tsuchiya, F., Sakanoi, T., et al. 2014, *SSRv*, **184**, 259
- Yoshikawa, I., Yoshioka, K., Murakami, G., et al. 2014, *SSRv*, **184**, 237